Biosensors and Bioelectronics 260 (2024) 116433

Contents lists available at ScienceDirect

Biosensors and Bioelectronics

journal homepage: www.elsevier.com/locate/bios

Controllable ion design in flexible metal organic framework film for performance regulation of electrochemical biosensing

Jinlong Wang [a,d,e], Ji Tan [f], Zhe Zhao [b,**], Jiayuan Huang [a,d,e], Junjie Zhou [f], Xinyi Ke [a,c,d,e], Zihan Lu [a], Gaoshan Huang [a,d,e,*], Hongqing Zhu [a,f], Xuanyong Liu [b,f,***], Yongfeng Mei [a,c,d,e]

[a] Department of Materials Science & State Key Laboratory of Molecular Engineering of Polymers, Fudan University, Shanghai, 200438, PR China
[b] College of Biological Science and Medical Engineering, Donghua University, Shanghai, 201620, PR China
[c] Shanghai Frontiers Science Research Base of Intelligent Optoelectronics and Perception, Institute of Optoelectronics, Fudan University, Shanghai, 200438, PR China
[d] Yiwu Research Institute of Fudan University, Yiwu, 322000, Zhejiang, PR China
[e] International Institute of Intelligent Nanorobots and Nanosystems, Fudan University, Shanghai, 200438, PR China
[f] State Key Laboratory of High Performance Ceramics and Superfine Microstructure, Shanghai Institute of Ceramics, Chinese Academy of Sciences, Shanghai, 200050, PR China

ARTICLE INFO

Keywords:
Ion design
Metal-organic framework film
Performance regulation
Area-selective patterning
Electrochemical biosensing

ABSTRACT

The limitations of solvent residues, unmanageable film growth regions, and substandard performance impede the extensive utilization of metal-organic framework (MOF) films for biosensing devices. Here, we report a strategy for ion design in gas-phase synthesized flexible MOF porous film to attain universal regulation of biosensing performances. The key fabrication process involves atomic layer deposition of induced layer coupled with lithography-assisted patterning and area-selective gas-phase synthesis of MOF film within a chemical vapor deposition system. Sensing platforms are subsequently formed to achieve specific detection of H_2O_2, dopamine, and glucose molecules by respectively implanting Co, Fe, and Ni ions into the network structure of MOF films. Furthermore, we showcase a practical device constructed from Co ions-implanted ZIF-4 film to accomplish real-time surveillance of H_2O_2 concentration at mouse wound. This study specifically elucidates the electronic structure and coordination mode of ion design in MOF film, and the obtained knowledge aids in tuning the electrochemical property of MOF film for advantageous sensing devices.

1. Introduction

The urgent demand for long-term real-time monitoring of skin surface components such as H_2O_2, glucose, dopamine (DA), and other biomolecules for wound healing monitoring, aging, and chronic disease management has promoted the development of flexible sensing devices that can be fitted to the skin (Hao et al., 2022; Shi et al., 2021; Yao et al., 2023). For example, real-time monitoring of the degree of healing of chronic wounds can be achieved by monitoring the concentration of hydrogen peroxide (H_2O_2) at the wound site (Hao et al., 2021). When skin injury occurs, leukocytes and other cells in the tissue surrounding the wound release H_2O_2 (Yoo et al., 2011). Its powerful oxidation and anti-inflammatory abilities can disinfect wound tissue (Lisse and Rieger, 2017). As the wound heals slowly, the concentration of H_2O_2 at the wound decreases (Cui et al., 2021). But it still helps to remove pathogens and bacterial debris, and promotes the synthesis and secretion of cytokines (Raval et al., 2023). Eventually, H_2O_2 disappears with the complete healing of the wound (Yoo et al., 2011). Compared to other reactive oxygen species in the organism, H_2O_2 is relatively stable, allowing it to act as a target molecule for detection (Zhang et al., 2023b). In addition, it is worth noting that H_2O_2 concentration at chronic wounds is commonly below 10 μM and the diverse biomolecules may exist in environment (Kekonen et al., 2019), H_2O_2 sensor with low limit of detection (LOD), high sensitivity, and excellent selectivity is urgently needed to achieve real-time accurate monitoring of the healing of chronic wound (Hu et al., 2017).

* Corresponding author. Department of Materials Science & State Key Laboratory of Molecular Engineering of Polymers, Fudan University, Shanghai, 200438, PR China.
** Corresponding author.
*** Corresponding author. College of Biological Science and Medical Engineering, Donghua University, Shanghai, 201620, PR China.
E-mail addresses: zhezhao@dhu.edu.cn (Z. Zhao), gshuang@fudan.edu.cn (G. Huang), xyliu@mail.sic.ac.cn (X. Liu).

https://doi.org/10.1016/j.bios.2024.116433
Received 8 January 2024; Received in revised form 22 May 2024; Accepted 25 May 2024
Available online 27 May 2024

From the viewpoint of performance, traditional enzyme-based biomolecular sensing approach has good selectivity and anti-interference ability (Liu et al., 2023). However, natural enzymes have unsatisfied performance (e.g., low sensitivity and large LOD) and high cost, and are difficult to be long-term used in the devices (Schelch et al., 2022). The design of efficient non-enzymatic biosensors becomes crucial (Xia et al., 2024). For non-enzymatic biosensors, the design of functional components of the sensors is the most important aspect to be investigated (Ahmad et al., 2022). Metal organic frameworks (MOFs) has a large specific surface area, abundant active sites, and stable properties, suggesting them suitable for enzyme-free sensing of biomolecules, and therefore MOF-related materials have recently attracted extensive attention (Zhao et al., 2022; Wang et al., 2022). However, the sensing application of MOFs is so far still limited because that the sensing targets and sensing properties are closely related to metal ions and crystal structures (Chen et al., 2022c; Fu et al., 2023). Modulation of metal ions in MOFs by post-treatment has become an important way to expand their applications (Ji et al., 2018; Chen et al., 2022b). The simple mixing of the synthesized MOF with other components is a primary means of post-treatment, which enables the combined performance of MOF and added components (Zhang et al., 2023a). However, the post-added components are not firmly attached to MOF and have poor performance stability (Jo et al., 2023). Pang et al. used ethanol to change the coordination mode on the surface of ZIF-67 and insert Ni ions into the Co-MOF (Zhou et al., 2023). However, the method is not universal, and the interaction between the newly added metal ions and the original MOF is unclear, which may influence the performance optimization. Thus, it is still challenging to carry out efficient ion design in MOF-related materials and to tune the properties of MOF films correspondingly for advantageous bio-sensing device. We consider that ZIF-4 with high stability, easy structural modification, and poor specific response to biomolecules is an appropriate platform to study the effect of ion regulation of the film via an ion implantation process (Shi et al., 2023b).

Herein, we propose to synthesized uniform and controllable ZIF-4 film through all-gas-vapor deposition. Further, we used photolithography to area-selectively pattern the ZIF-4 films in order to create practical sensor devices on flexible substrates. In order to modulate the sensing properties of all-gas-vapor deposited MOF films on sensor devices, we propose a strategy of metal ions design in MOF films by plasma immersion implantation of Co, Fe, and Ni ions. The doses/concentraions of the ions introduced were precisely controlled via tuning the implantation time. The modified MOF films were then used for the specific sensing. To assess the impact of implanted metal ions on the sensing performance, we investigated the state of metal ions in ZIF-4 and the interaction between implanted metal ions and ligands. The results indicated that the metal ions are chemically bonded to N atoms and anchored to the ZIF-4 network. Our study confirms that the metal ions implanted enhance the biomolecule adsorption on MOF and reduce the activation energy barrier, thus greatly promoting the sensing performance. This work provides the theoretical and experimental bases for the integrated device applications of MOF films.

2. Experimental section

2.1. Materials

Ecoflex 00–30 was purchased from Smooth-On. Carbon black powder (Super P Li) was purchased from TIMCAL. Cyclohexane (AR, ≥99.5%). Hydrogen peroxide (30%), D-(+)-Glucose monohydrate (AR, ≥99.7%), potassium ferricyanide ($K_3[Fe(CN)_6]$), and lactic acid (AR, ≥99.7%) were purchased from Sinopharm Chemicals. Imidazole (≥99.5%), Nafion (5 wt%), dopamine hydrochloride (≥97%), sodium chloride (AR, ≥99.5%), potassium chloride (AR, ≥99.5%), hydrochloric acid (37%), acetone (AR, ≥99.5%), ethanol (AR, ≥99.7%), and PBS (pH 7.2) were obtained from Aladdin Ltd. (Shanghai, China). All the reagents were used as received, without further purification. The deionized water used in all experiments was purified by a Millipore system.

2.2. Preparation of conductive flexible Ecoflex substrate

Part A and part B of Ecoflex 00–30 (ratio 1:1) were added into two beakers. Abrasive carbon black powder from the agate mortar was added into the beakers of part A and part B (ratio 1:18). The mixtures were stirred thoroughly and dispersed well under ultrasonication. Afterwards, the samples were placed in a vacuum drying oven for 10 min to release air bubbles. The viscosities of the solutions were adjusted by adding cyclohexane ($CH_2(CH_2)_4CH_2$) into the beakers containing part A and part B (the volume ratio of part A/B to cyclohexane is 1:5). The diluted Part A and part B were then mixed and spin-coated on glass substrate to form a film of about 20 μm thickness. The samples were cured at 60 °C for 12 h to form conductive flexible Ecoflex substrates.

2.3. Preparation of ZnO nanomembrane by ALD

The deposition of ZnO nanomembrane on flexible Ecoflex films was performed by atomic layer deposition (ALD). The deposition process was carried out in our self-built ALD chamber at 120 °C. Diethylzinc (DEZ) and deionized water were used as precursors. A typical ALD cycle process includes DEZ pulse (50 ms), wait (5 s), N_2 purge (20 s), DI water pulse (50 ms), wait (5 s), and N_2 purge (20 s). Samples with different numbers of ALD cycles were prepared in order to investigate the influence of the thickness of ZnO nanomembrane.

2.4. Preparation of patterned ZnO nanomembrane

The silicon substrate or flexible Ecoflex film was first coated with ZnO nanomembrane by using ALD. A uniform photoresist (ARP-3510, Allresist GmbH) layer with a thickness of approximately 2 μm was spin-coated on the sample surface. The photoresist layer was then patterned by UV lithography (SUSS MA6). Next, the exposed ZnO nanomembrane was etched off by diluted HCl (5 mM). Afterwards, the photoresist layer was removed with organic solvent. Patterned ZnO nanomembrane was used to induce the assembly of MOF film.

2.5. Gas-phase synthesis of patterned ZIF-4 films on flexible devices

The synthesis of MOF films was performed in a self-made chemical vapor deposition (CVD) system equipped with a 150 cm horizontal tube furnace and a 3-inch inner diameter quartz tube. The imidazole powder ground in an agate mortar was used as an evaporation precursor to synthesize the ZIF-4 films. The imidazole powder was placed at the center of the furnace, and the substrate with ZnO nanomembrane was placed at 5 cm directly above the imidazole powder. The heat source temperature was maintained at 120 °C for 6 h. High purity N_2 gas was used as the carrier gas with a typical flow rate of 80 sccm, and the total pressure in the system was kept at 300 torr. To investigate the growth mechanism, reference samples with different reaction temperatures were also prepared.

2.6. Ion immersion implantation of metal ions

ZIF-4 film were placed inside the ion implanter cavity. High purity Co, Fe, and Ni targets (≥99.95%) were used in this work. The implantation voltage was set to −500 V, and the amounts of ions implanted was controlled by adjusting the implantation time. During ion immersion implantation, the sample stage is cooled to approximately 25 °C by circulating water.

2.7. Preparation of wound H_2O_2 concentration sensor

Conductive Ecoflex flexible substrate was cut into a rectangle with an

area of 9 × 10 mm^2. A uniform photoresist (ARP-3510, Allresist GmbH) layer with a thickness of approximately 2 μm was spin-coated on the substrate surface. The photoresist layer was then patterned into designed shape by UV lithography (SUSS MA6). Then, 10 nm Ge film and 50 nm Au film were deposited by using magnetron sputtering. Afterwards, photoresist layer was removed and patterned Ge/Au electrodes were obtained. ZnO nanomembrane was deposited by ALD with 300 cycles, and then patterned to fit the working Ge/Au electrode. Subsequently, ZIF-4 film was synthsized in ZnO area by the CVD process to realize the precise coverage of Ge/Au working electrode. The wound H_2O_2 concentration sensor was finally produced after the Co ion implantation.

2.8. Structural characterization

The thickness of the ZIF-4 film was obtained by using a profilometer (Bruke Dektak XT). The morphologies of all samples were recorded by field emission scanning electron microscopy (SEM, ZEISS Sigma 300). Energy dispersive spectrometer (EDS, Oxford Xplore 30) was used to analyze the composition and ion concentration of the samples. XPS analyses was performed by using Thermo Scientific K-Alpha equipment. Curve fitting of all XPS spectra was complete by using XPS Peak 4.0 software. XRD patterns were measured by an X'Pert ProX-ray diffractometer equipped with Cu Kα radiation (λ = 0.1542 nm) at 40 mA and 40 kV. TGA was performed by using a PerkinElmer STA 6000 instrument in the air atmosphere with a 10 °C min^{-1} warming rate. Raman spectra were obtained on a Renishaw inVia spectrometer under excitation of a 532 nm laser. A Micromeritics APSP 2460 was used to perform nitrogen adsorption/desorption measurements. The specific surface area was calculated by using the single point Brunauer-Emmett-Teller (BET) method. Pore size distributions were calculated from nitrogen adsorption data by using the Barrett Joyner Halenda (BJH) and DFT method provided by Quantachrome data reduction software ASiQwin Version 4.01.

2.9. Electrochemical characterization

Electrochemical sensing tests were evaluated on a CHI660E (Chenhua Instrument, Shanghai, China) electrochemical work station with a three-electrode configuration. In our experiments, an Ag/AgCl (in saturated KCl solution) was used as the reference electrode and a graphite rod was applied as the counter electrode. The ZIF-4 film with intended ion design on the conductive Ecoflex was directly used as the working electrode. In this work, the samples were tailored into a rectangle with an area of 9 × 10 mm^2 for the working electrode.

2.10. In vitro biocompatibility assay

The culture medium used in the experiment was α-MEM media (Gibco, Invitrogen Inc), supplemented with 10% fetal bovine serum (FBS, USA),1% antimicrobial penicillin and streptomycin (USA). In order to check the biocompatibility of the Co-PFM-30, Co-PFM-30 extract was prepared by immersing Co-PFM-30 in 1 mL of blank culture medium for 24 h, and then filtering the culture medium with a sterile 0.22 μm filter head. Mouse fibroblasts (L929) cells provided by Cell Bank, Chinese Academy of Sciences, were cultured at 37 °C in an incubator (5% CO_2 and 95% relative humidity). Specifically, L929 cells (5×10^3 cells/well, 100 μL) were inoculated with blank culture medium in 96-well plates for 6 h. Afterwards, the culture medium was replaced with an equal amount of extract. The incubation was continued in the medium for 24 and 48 h and then 120 μL of medium containing 10% alamarBlue™ (Invitrogen, USA) was added to each well for additional incubation of 2 h. The fluorescence intensity was detected by a Microplate Reader (Cytation 5, BioTek, USA) with excitation wavelength of 560 nm and emission wavelength of 590 nm. Cell viability was assessed by using a live/dead cell staining kit (Biovision, USA). Specifically, L929 cells (5.0×10^3 cells/mL) were cultured with Co-PFM-30 extract for two days. Then, 100 μL fresh PBS with calcein-AM and propidium iodide was introduced for another 30-min incubation. Finally, fluorescent photograph was obtained by using a fluorescence microscope (Olympus, Japan). For biocompatibility assessment, L929 cells were also cultured with just blank culture medium in the experiment while other processes are the same.

2.11. Creation and detection of animal wound model

The animal models used were approved by the Experimental Animal Ethics Committee of Kangtai Medical Laboratory Services Hebei Co. (Approval number: MDL2023-06-11-01) in accordance with the relevant regulations for animal experiments. Healthy adult male mice (~300 g) were selected as the measurement subjects. Before surgery, the mouse was anesthetized by intraperitoneal injection of chloral hydrate with a dose of 350 mg kg^{-1} animal body weight. The mouse was then fixed on a stereotaxic apparatus. The fur on it dorsum was scraped from the skin and the epidermis was cut open to create a full-thickness skin wound. The prepared H_2O_2 sensor was attached to the wound for current detection. The control group model was conducted by adding 0.1 M PBS onto the posterior back skin of mouse without wound.

3. Results and discussion

Fig. 1a shows a schematic diagram of the preparation process of porous flexible film (PFM, i.e., MOF film) and Co ions-implanted PFM (Co-PFM). In order to achieve the flexibility, conductivity, and biocompatibility of the resultant film, a carbon black (5 wt%) modified Ecoflex film is served as substrate. A uniform ZIF-4 film is deposited on the surface of Ecoflex film as a platform for active materials. To further diminish the corrosive effect of solvent residues and applied this strategy for device production, the pure gas-phase fabrication of ZIF-4 film is adopted by combining ALD and CVD approaches. Specifically, a ZnO nanomembrane is firstly deposited on the surface of substrate (i.e., Ecoflex film) by ALD as an induction layer. Then, ZIF-4 film is formed in the gaseous atmosphere of imidazole ligands by using a homemade CVD system. In order to investigate the appropriate temperature for the syntheses of ZIF-4 film, the cavity temperature of the CVD system is adjusted from 100 to 140 °C. As shown in Fig. S1, at relative low temperature of 100 °C and high temperature of 140 °C, an unsatisfied ZIF-4 film is formed as a scattered disperse of ZIF-4 particles is noticed. A uniform ZIF-4 film is observable at a moderate temperature of 120 °C. This phenomenon can be explained as that at high temperature the ZIF-4 crystals are incline to collapse, while at low temperature the crystals are hard to nucleate (Widmer et al., 2019). It should be noted that the thickness of ZIF-4 film can be controlled by adjusting cycle number of ALD process, which changes the thickness of ZnO nanomembrane (Fig. S2). For instance, ZIF-4 film thickness increases from 460 to 820 nm as the number of ALD cycles increases from 200 to 400.

In order to pattern the MOF film for device, area-selective growth is a prerequisite. Using a precise assembly technique with lithographically patterned ZnO nanomembrane as induction layer, we achieve precise assembly of MOF crystals in specified regions of the substrate during the ligand gas-phase reaction (Fig. 1b and Fig. S3), and the pattern of ZIF-4 film well duplicates that of ZnO nanomembrane. It can be clearly seen that C and Zn elements are uniformly dispersed on the substrate except for the "FDU" pattern, because of the uniform distribution of ZIF-4 crystals. The coverage of ZIF-4 film makes the distribution of Si content opposite to that of Zn content.

In order to realize biosensing of ZIF-4 platform which is intrinsically not applicable for electrochemical sensing, a designable ion regulation is achieved by ion implantation (Fig. 1a and c). In current approach, versatile functional ions including Co, Fe, and Ni can be implanted and anchored on the period network of ZIF-4 film. Obviously, the amount of ions in the modified ZIF-4 film should be closely related to the

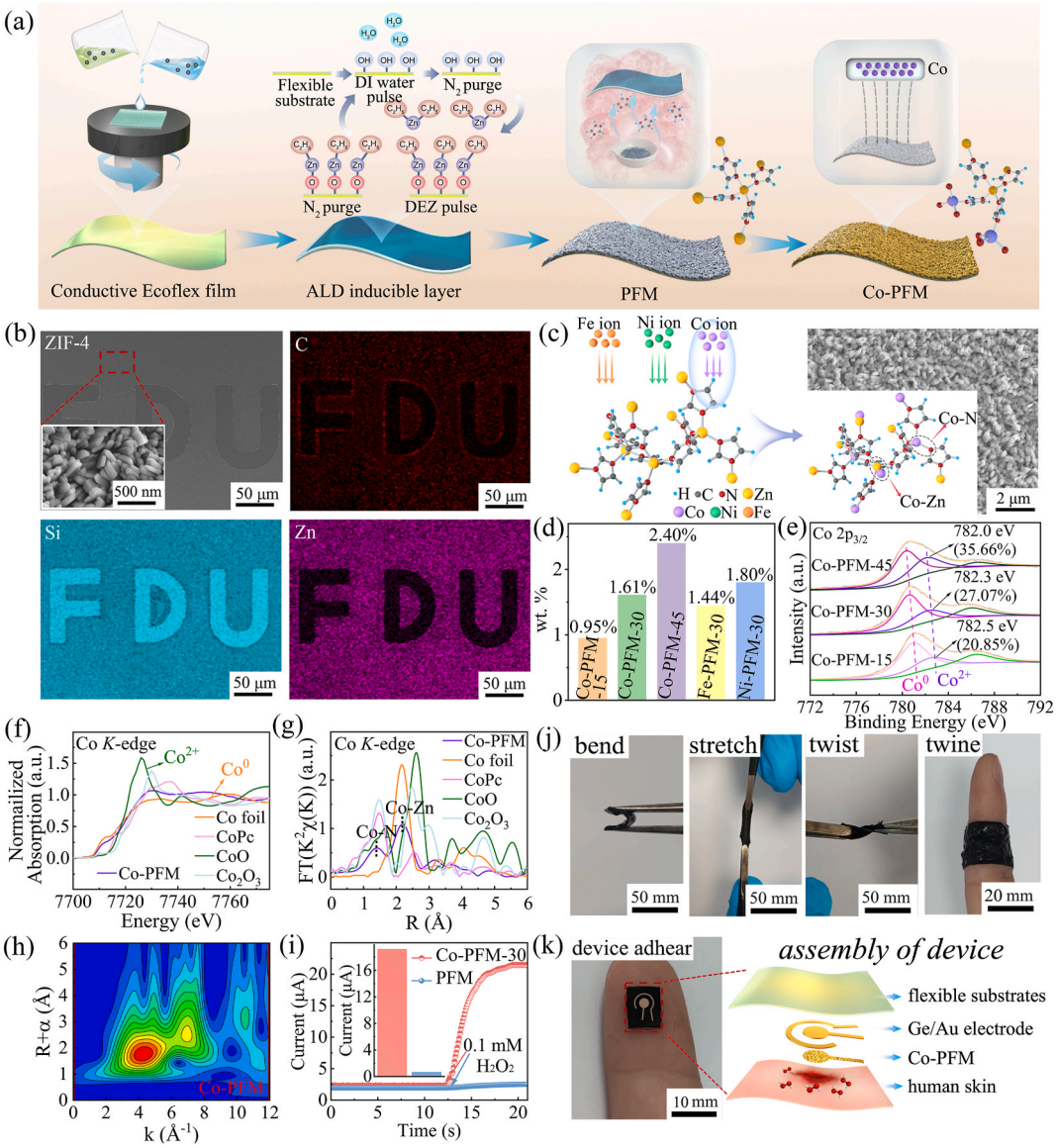

Fig. 1. Area-selective preparation of porous flexible sensing platforms with controllable ion design and investigation of ion coordination mode. (a) Preparation process of Co-PFM film synthesized by pure gas-phase method. (b) SEM images and EDS mapping of patterned ZIF-4 film (ZIF-4 crystals are assembled in area outside the "FDU" pattern). (c) Schematic of the ZIF-4 film with metal ions implanted and SEM image of Co-PFM-30. (d) Mass fraction of elements in PFM film after implantation of Co, Fe, and Ni. (e) High-resolution XPS $Co2p_{3/2}$ spectra of Co-PFM film with different implantation times. (f) Co K-edge XANES spectra of Co-PFM film and references. (g) FT k^3-weighted EXAFS spectra of Co-PFM-30 film and references. (h) WT analysis of Co-PFM-30 film. (i) The response currents of PFM and Co-PFM-30 for 0.1 mM H_2O_2 in 0.1 M PBS at 0.6 V. The inset shows the comparison of the response currents. (j) Demonstration of the flexibility of Co-PFM-30 film under bending, stretching, twisting, and twine. (k) Photograph and structural schematic of the wound H_2O_2 concentration sensor prepared by using Co-PFM-30 as active material.

implantation time. In order to confirm this tunability, Co-PFM with ion implantation times of 15, 30, and 45 min (denoted as Co-PFM-15, Co-PFM-30, and Co-PFM-45, respectively), Fe-PFM with ion implantation time of 30 min (denoted as Fe-PFM-30), and Ni-PFM with ion implantation time of 30 min (denoted as Ni-PFM-30) were fabricated and characterized. Fig. S4 shows the EDS mapping of Fe, Ni, and Co ions anchored on ZIF-4 film and a typical EDS spectrum of Co-PFM-30. The results demonstrate that the high-energy ions are successfully introduced into the ZIF-4 film, and the amount of the ion indeed increases with the increased implantation time (Fig. 1d), which is a crucial for the realization of the ion design in the proposed biosensing platform, as will be discussed later. Moreover, Fig. 1c shows the SEM image of Co-PFM-30 and the schematic of the structure. The ZIF-4 film on the flexible substrate with Co ions implanted is uniform and the morphology is similar to that of ZIF-4 particles synthesized by conventional hydrothermal method (Fig. S5). We also note that the ion implantation did not produce significant changes of the morphology (Figs. S6 and S7).

According to the literature, in the resultant Co-PFM, Co ions may anchor on ZIF-4 network by two manners (inset in Fig. 1c) (Zuo et al., 2023). In the first manner, Co ion takes the place of Zn ion and form the Co–N coordination bond (Shi et al., 2023a). On the other hand, Co–Zn covalent bond may form, which co-coordinates with the original organic frameworks (Li et al., 2023a). To further investigate the chemical state and bond structure of Co-PFM, X-ray photoelectron spectroscopy (XPS) spectra of Co-PFM samples with different Co implantation times were measured and the results (Fig. 1e and Fig. S8) confirm the presence of Co, Zn, O, and C in all the samples. The high-resolution $Co2p_{3/2}$ spectrum shown in Fig. 1e can be deconvoluted into three peaks at 780.5, 782.3, and 786.0 eV, corresponding to Co^0, Co^{2+}, and satellite species, respectively (Hu et al., 2023). The detailed proportion can be obtained

by peak fitting of the spectra, and we find that if the implantation time increases from 15 to 45 min, an increase in Co^{2+} proportion from 20.85% to 35.66% can be obtained. That is, longer implantation time causes higher Co^{2+} concentration and more active sites are introduced for following biosensing (Li et al., 2022). Moreover, the valence of Co within the Co-PFM-30 is probed by X-ray absorption near-edge structure (XANES) spectrum, as shown in Fig. 1f. The normalized Co K-edge XANES curve shows that the absorption edge of Co-PFM-30 is located between Co foil and CoO, indicating that the valence of Co ions implanted into ZIF-4 crystals is between Co^0 and Co^{2+} (Sarmah et al., 2022). The Fourier transform (FT) k^3-weighted extended X-ray absorption fine structure (EXAFS) spectra of the Co-PFM-30 compared with Co foil, CoPc, CoO, and Co_2O_3 samples are displayed in Fig. 1g (in R space) and Fig. S9 (in k space). Two apparent peaks locate at 1.41 and 2.20 Å can be clearly observed, which are attributed to the scattering of Co–N and Co–Zn bonds, respectively (Chen et al., 2022a). To further confirm the existence of Co–N and Co–Zn bonds, the wavelet transform (WT) analysis on the k^3-weighted Co K-edge EXAFS signal was carried out and

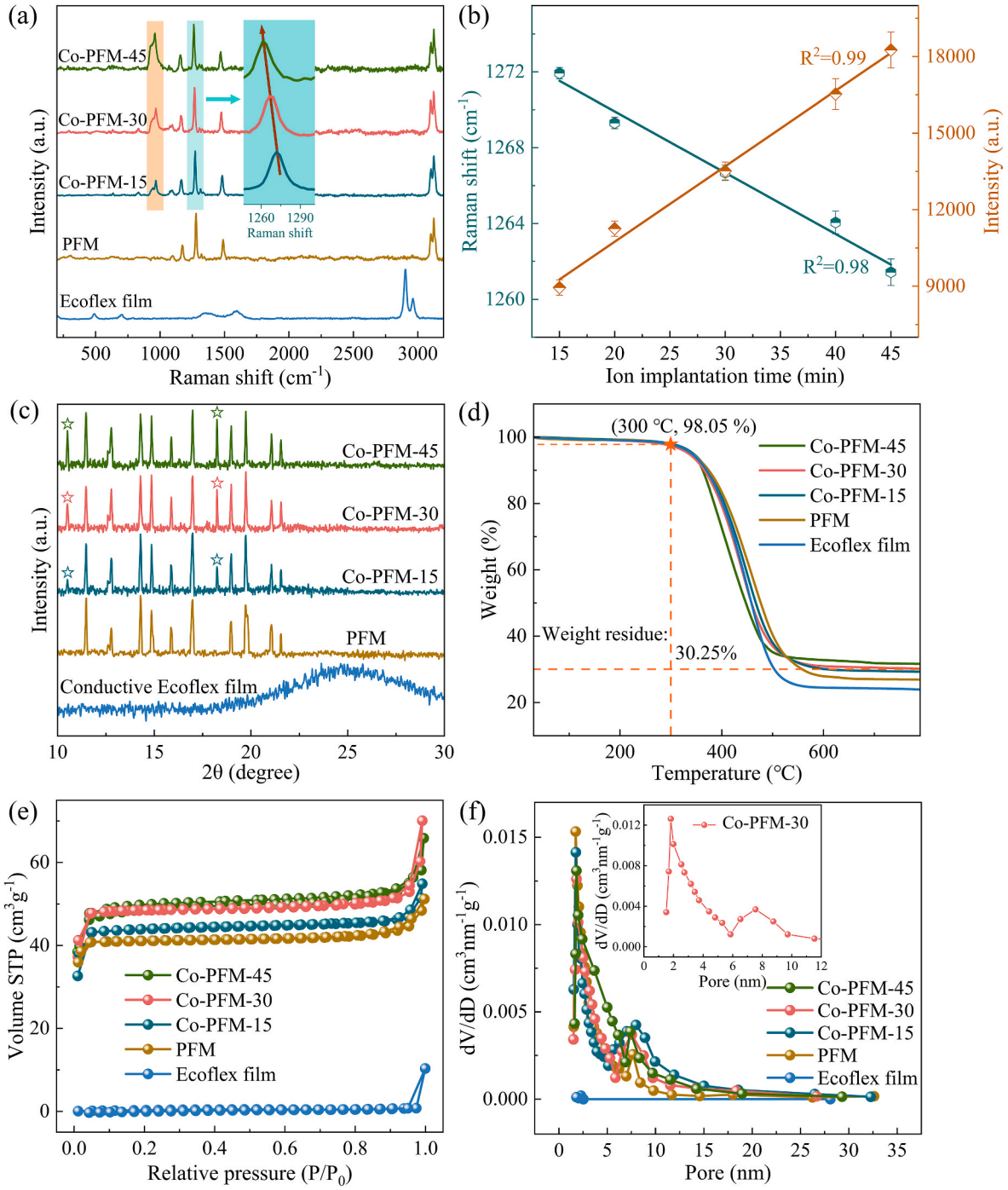

Fig. 2. Structural characterization of porous flexible films with ion design. (a) Raman spectra of conductive flexible Ecoflex films, PFM, and Co-PFM with different Co ion implantation times. (b) The shift of the Raman peaks at 1275 cm^{-1} and the intensity of the Raman peak at 967 cm^{-1} as functions of the implantation time. (c) XRD patterns of the samples. The asterisks represent the peaks arise after Co ion implantation. (d) TGA curves of the samples. The asterisk represents the temperature point below which the structure of the samples are stabilized. (e) Nitrogen adsorption-desorption isotherms and (f) corresponding pore size distribution of the samples.

the results are shown in Fig. 1h. Compared with the results of Co foil and CoPc (Fig. S10), a WT K-edge intensity maxima located at 4.1 $Å^{-1}$ is ascribed to CoPC, indicating a Co–N bond scattering (Elanjeitsenni et al., 2022). More importantly, no Co–Co bond at 6.6 $Å^{-1}$ can be seen in Co-PFM-30. Considering the Co^0 state in XANES, we may infer the existence of Co–Zn bond, as schematically shown in Fig. 1c. In addition, the specific structural parameters of Co–N and Co–Zn bonds in Co-PFM-30 are investigated by atomic oscillation and FT-EXAFS fitting (Fig. S11 and Table S1), and a good fitting further confirms the existence of Co–N and Co–Zn bonds in Co-PFM-30.

We find that such Co ions anchored on the ZIF-4 organic framework network structure through Co–N coordination bonds and Co–Zn covalent bonds lead to noticeable electrochemical sensing ability towards H_2O_2 (Fig. 1i), and the mechanism will be explained later. In addition, the sensing performance changes with the film thickness, as shown in Fig. S12. The thinner film demonstrate poor performance due to fewer active sites (Majhi et al., 2022), while excessively thick MOF film leads to poor conductivity for ion transport, reducing the sensing performance (Zhao et al., 2018). 630 nm thick Co-PFM-30 film induced by ZnO nanomembrane of 300 ALD cycles is believed to be the best, and will be used in the following investigations. Fig. 1j demonstrates the flexibility of the prepared Co-PFM-30 under bending, stretching, and twisting and the film can tightly adhere on the human skin. The SEM image of Co-PFM-30 after 50 bending cycles with a curvature radius of 10 mm is shown in Fig. S13, and no significant crack is observed. These results demonstrate the robust mechanical integrity and skin conformability of the Co-PFM films under various expected deformations corresponding to the wearer's daily activities. By means of area-selective assembly of MOF film and photolithography technique, we realize precise coverage of Ge/Au working electrode by ZIF-4 film on flexible Ecoflex substrate, and a specific sensing device for skin surface biomolecules is prepared. Fig. 1k shows a photograph and structural schematic of the Co-PFM-based sensing device for wound monitoring. Ultimately, the preparation of this flexible sensor device achieves accurate sensing of practical H_2O_2 concentration, and it have great potential in monitoring wound healing, as will be discussed later.

The structures of ZIF-4 film and Co-PFM on flexible Ecoflex substrates are further investigated. Fig. 2a shows the Raman spectra of the samples. Ecoflex film exhibit typical D, G, and 2D bands at 1350, 1590, and 2900 cm^{-1}, attributed to defects and primary and secondary vibrations of the C–C bond, respectively (Li et al., 2023b). The peaks at 479 and 702 cm^{-1} may originate from the silicone rubber in Ecoflex (Zhang et al., 2023c). The Raman scattering of PFM sample demonstrates peaks at 1169, 1275, and 1487 cm^{-1}, which is consistent with the results reported in the literature for ZIF-4 crystals synthesized by solvothermal method (Jain et al., 2023). One can see that the Co ion implantation results in an additional peak at 967 cm^{-1}. Combined with the XPS and synchrotron radiation results in Fig. 1, it is speculated that this peak is connected with Co–N structure (Li et al., 2021a). In addition, the amount of implanted Co ions also leads to shift of ZIF-4 characteristic peaks (e.g., the peak at 1275 cm^{-1}). Fig. 2b quantitatively demonstrates the relationship between the amount of Co ions and the shift of the Raman peak at 1275 cm^{-1} as well as the intensity of the peak at 967 cm^{-1}. The fitting results show that the 1275 cm^{-1} peak shifts to lower wavenumber linearly with the increase of amount of Co ions. This may be attributed to transition of Zn–N–C–N–Zn in the original ZIF-4 crystal to Zn–N–C–N–Co due to the implantation of Co ions (Geng et al., 2023). In addition, the intensity of the Raman peak at 967 cm^{-1} linearly intensifies with amount of Co ions, suggesting that the quantification of Co ions in the Co-PFM films can be realized non-destructively and rapidly via monitoring the evolution of the Raman peaks. In order to investigate the crystal structure of the samples, X-ray diffraction (XRD) patterns are measured and the results are shown in Fig. 2c. The broad band at 20°~30° from conductive Ecoflex films can be attributed to the amorphous structure of the organic components (Albetran, 2023). After the growth of PFM, several sharp peaks appear which are related to ZIF-4 structure (Shahsavari et al., 2023), confirming the feasibility of synthesizing ZIF-4 film by current pure gas-phase method. It should be noted that after the implantation of Co ions, XRD patterns of Co-PFM changes compared to that of PFM, with the appearance of two new sharp peaks located at 10.5° and 18.2° (marked by the asterisks in Fig. 2c). These new peaks are presumably attributed to Co-related crystal structure embedded in PFM (Ghafoor et al., 2023), and the intensity of the peaks is positively correlated with the amount of Co ions implanted. Thermal stability of the samples is also characterized by Thermogravimetric analysis (TGA). As shown in Fig. 2d, the masses of the samples decreases by only ~2 % below 300 °C. A gradual decrease in mass can be seen at temperatures higher than 300 °C, which is caused by the oxidative degradation of the organic linker and the carbon material (Zhao et al., 2020). This result illuminates the excellent structural stability of Co-PFM over a wide temperature range. We also specifically investigated the pore structure of the samples. Fig. 2e and f show the nitrogen adsorption-desorption isotherms and the corresponding pore size distribution of the samples, respectively. For a more accurate estimation of micropore distribution, Density Functional Theory (DFT) model was also engaged and the results are shown in Fig. S14. According to these characterizations, the conductive Ecoflex film exhibits a negligible porous structure with a negligible specific surface area of 1.64 m^2g^{-1}. In contrast, PFM exhibits a Type I isotherms with a large surface area of 184 m^2g^{-1}. It is worth noting that the pore size calculation reveals the presence of not only significant micropores with a size of 1.28 nm, but also some mesopores with a size of 7.67 nm in the PFM. This phenomenon implies the existence of a porous structure consisting of micropores and mesopores (Calzaferri et al., 2022). We consider that the presence of mesopores can be attributed to the close accumulation of ZIF-4 particles in the film (Liu and Hudson, 2023). The detailed pore structure of the sample is summarized in Table S2. One can see that the pore structure of Co-PFM with different amounts of Co ions are consistent with that of original PFM, indicating that the ion implantation did not destroy the porous structure. It is worth noting that the unique porous structure of Co-PFM samples can promote the permeation of biomolecules for enhanced sensing performance (Rezki et al., 2022), as will be discussed later.

To determine application potential of PFM with intended ion design in biosensing, the PFM samples were used as electrode for electrochemical sensing and the performances were specifically investigated. Fig. S15 shows the effect of the applied potential on the current response of Co-PFM-30 in 0.1 M PBS containing 1 mM H_2O_2. It is clear that at 0.6 V, the Co-PFM exhibited a significant and stable response. In addition, Fig. S16 shows the current response of Ecoflex film with 30-min Co ion implantation towards 100 μM H_2O_2, and a negligible current response is noticed. This can be explained as the Ecoflex film does not possess porous structure, and Co ions are embedded inside the bulk Ecoflex film, making it impossible for H_2O_2 molecules to effectively contact the active Co ions. To evaluate the application of the Co-PMF with different amounts of Co ions for H_2O_2 sensing, we measured the sensing performance of Co-PFM with different implantation times. Fig. 3a shows the response currents of Co-PFM with different Co ion implantation times in 0.1 M PBS with addition of 1 mM H_2O_2 at a voltage of 0.6 V. And the inset shows the i-t tests of Co-PFM-15, Co-PFM-30, and Co-PFM-45 with addition of 1 mM H_2O_2 for two consecutive times compared with that of PFM. The results demonstrate that the PFM is insensitive to H_2O_2. While after Co ion implantation, the Co-PFM-30 exhibits a significantly increased current response, and the current response of the Co-PFM increases with increased implantation time (i.e., amount of Co ions). However, when the Co ion implantation time exceeds 30 min, the increase of electrochemical response tends to be saturate, and a decrease is even observable with elongated implantation time. In addition, the error bar increases rapidly when the implantation time is beyond 30 min. The response saturation may be due to the fact that the sites left for Co–N, Co–Zn co-location within the ZIF-4 film crystal are limited, and active site cannot continuously increase with more Co ions implanted (Xie

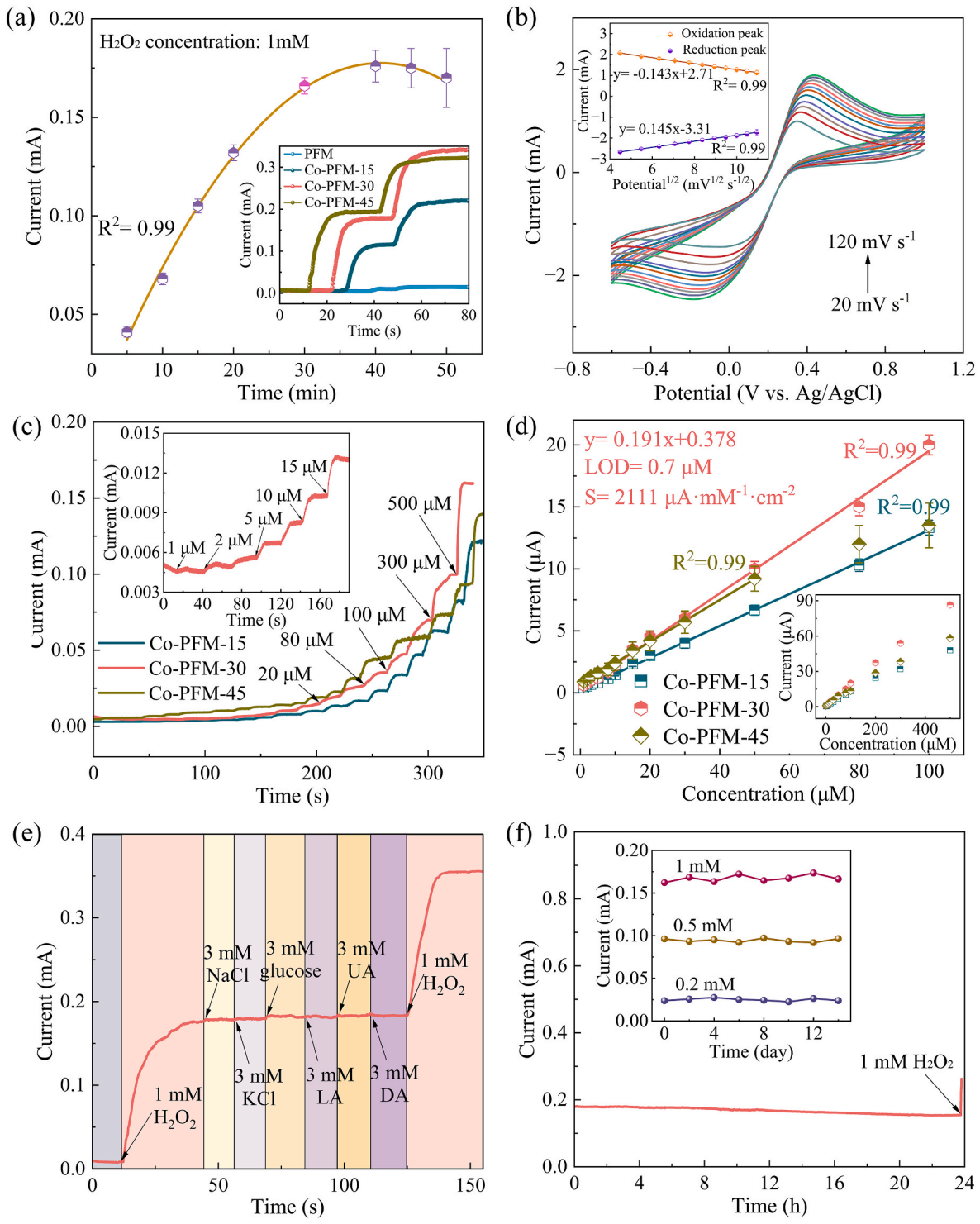

Fig. 3. Sensing performance of porous flexible film. (a) Response currents of Co-PFM in 0.1 M PBS containing 1 mM H_2O_2 at 0.6 V as a function of Co ion implantation time. The inset shows the response currents of samples with and without Co ion implantation for two consecutive additions of 1 mM H_2O_2 in 0.1 M PBS at 0.6 V. (b) CV scans of Co-PFM-30 in 0.1 M PBS at various scan rates of 30–120 mV s^{-1} in 0.1 M PBS containing 5 mM $K_3[Fe(CN)_6]$. (c) i-t curve of Co-PFM with different Co ion implantation times for the successive addition of H_2O_2 in 0.1 M PBS at 0.6 V. The inset is the amplified i-t curve of Co-PFM-30 for the successive addition of H_2O_2 with concentrations below 20 μM. (d) Responses as functions of H_2O_2 concentration (linear region, up to 100 μM) for Co-PFM with different Co ion implantation times. The inset shows corresponding responses as functions of H_2O_2 concentrations up to 500 μM. (e) i-t curve of Co-PFM-30 in 0.1 M PBS with successive addition of 1 mM H_2O_2, 3 mM NaCl, 3 mM KCl, 3 mM glucose, 3 mM LA, 3 mM UA, 3 mM DA, and 1 mM H_2O_2 at 0.6 V. (f) i-t curve of Co-PFM-30 in 0.1 M PBS with 1 mM H_2O_2 at 0.6 V. 1 mM H_2O_2 was added to the solution after 24 h to test the performance recovery. The inset shows the response currents of Co-PFM-30 in 0.1 M PBS containing 0.2 mM, 0.5 mM, and 1 mM H_2O_2 measured every 2 days at 0.6 V.

et al., 2022). On the other hand, the decreased response and the increased error bar may be due to the long-time bombardment in the case of implantation, which leads to certain structural damage of the network (Yuan et al., 2023). Therefore, we believe that an ion implantation time of 30 min is the most appropriate for Co-PFM sample.

Next, we quantitatively investigate the electrochemical active area of Co-PFM-30, by using $K_3[Fe(CN)_6]$ as a probe. As shown in Fig. 3b–a pair of oxidation and reduction peaks can be observed in the CV scan of Co-PFM-30. And the oxidation and reduction peak currents increase as the scan rate increases from 20 to 120 mVs^{-1}. The actual active area (S) can be calculated by using Randles-Sevcik equation (Nisar et al., 2022): $I_{peak} = (2.69 \times 10^5)n^{3/2}SD^{1/2}Cv^{1/2}$, where n is the number of transferred electrons (1 in present case), D is the diffusion coefficient of $K_3[Fe(CN)_6]$ (6.5×10^{-6} cm^2 s^{-1} in present case), and C is the overall concentration of $K_3[Fe(CN)_6]$ (5 mM in present case). According to the fitting results in the inset of Fig. 3b, the slope of I-$v^{1/2}$ curve is 0.145 mA $mV^{-1/2}s^{1/2}$ for reduction peak. Therefore, the calculated S of Co-PFM-30 is 0.042 cm^2. On the other hand, the nominal area of Co-PFM-30 electrode is calculated to be 0.049 cm^2, based on the geometry of the patterned electrode. Thus the actual active area is determined to be ~86% of the nominal area, which a relatively high value compared with the results in literature (Liu et al., 2022; Biswas et al., 2020). This large active area may be attributed to the hierarchically porous structure of the sample, which can facilitate electrochemical sensing performance (Zhao et al., 2019). Fig. 3c shows the current response of the Co-PFM samples in 0.1 M PBS with the successive addition of H_2O_2 at a potential of 0.6 V. After exposure to H_2O_2, a significant and rapid current response can be seen, indicating a real-time sensing capability. On the basis of the experimental results, the corresponding calibration plots of Co-PFM samples are shown in Fig. 3d. According to the calibration plots, Co-PFM-30 exhibits a high sensitivity of 2111 μA mM^{-1} cm^{-2} with a wide leaner range of 1–100 μM (linear regression equation: y = 0.191x+0.378; correlation coefficient (R^2 = 0.99)). The limited of detection is calculated to be 0.31 μM (based on S/N = 3 (Kim et al., 2018)). For comparison, Co-PFM-15 also has a linear relationship in the range of 1–100 μM, but with a lower sensitivity of 1449 μA mM^{-1} cm^{-2}, and Co-PFM-45 exhibits a linear relationship in the range of 1–50 μM with a sensitivity of 1858 μA mM^{-1} cm^{-2}. CV scans of Co-PFM-30 in 0.1 M PBS containing different concentrations of H_2O_2 are also used to evaluate the sensing performance. At high concentrations of 2–8 mM, as shown in Fig. S17, the oxidation peak current increases linearly with increased H_2O_2 concentration, and the sensitivity of Co-PFM-30 in the case of high H_2O_2 concentration is calculated to be 492 μA mM^{-1} cm^{-2}.

We notice that ZIF-4 film can be used as a general platform for electrochemical sensing of various biomolecules. In our work, we have explored not only Co ion implantation for H_2O_2 detection, but also implantation of Fe and Ni ions for DA and glucose sensing respectively. The characterizations (SEM, XRD, and XPS) of Fe and Ni ions anchored on the ZIF-4 network structure are shown in Fig. S18. Specifically, the mechanism of DA sensing of the Fe-PFM can be attributed to the following equations:

$$\text{Fe(III)-PFM-2e}^- + C_8H_9N(OH)_2 \rightarrow \text{Fe(II)-PFM} + C_8H_9NO_2 + 2H^+ \quad (1)$$

$$\text{Fe(II)-PFM} \rightarrow \text{Fe(III)-PFM} \quad (2)$$

And the mechanism of glucose sensing of the Ni-PFM can be explained as:

$$\text{Ni(II)-PFM} \rightarrow \text{Ni(III)-PFM} \quad (3)$$

$$\text{Ni(III)-PFM} + 2OH^- + C_6H_{12}O_6 \rightarrow \text{Ni(II)-PFM} + C_6H_{10}O_6 + 2H_2O + 2e^- \quad (4)$$

Figs. S19a and S20a respectively show the current responses of Fe-PFM-30 and Ni-PFM-30 for DA and glucose. The calibration curves of response currents versus concentration of target molecules are shown in the insets, and the results demonstrate good linearity in the range of 10–100 μM, and the sensitivities are 2475 and 1669 μA mM^{-1} cm^{-2} for DA and glucose with low LODs of 0.26 and 0.39 μM, respectively. Table S3 present detailed comparison of the performance of current sensor and those reported in the literature. We believe that the excellent sensing performance of the MOF films with specific ion designs can be attributed to the following factors. Firstly, the MOF films prepared by ALD and CVD are uniform, and the obtained films are firmly adhered to the substrate, providing a stable conductive pathway for ion transfer. Secondly, the hierarchical porous structure including mesopores and micropores leads to the exposure of more active sites and the penetration of the target molecules; Thirdly, the controllable and intended ion design of the MOF films remarkably increases the number of active sites, thus improving the sensing performance significantly.

For practical sensing application, other parameters like interference immunity, pH of environment, and stability are also important. In present work, H_2O_2 sensing by Co-PFM-30 was explicitly investigated as an example. Fig. 3e shows the i-t curve of Co-PFM-30 in 0.1 M PBS at 0.6 V for the sequential detections of 1 mM H_2O_2, 3 mM NaCl, 3 mM KCl, 3 mM glucose, 3 mM lactate (LA), 3 mM uric acid (UA), 3 mM DA, and 1 mM H_2O_2 as those are common interferents in wound fluids (Charkhabi et al., 2021). The i-t curve shows that the interferents produce small current responses compared to H_2O_2, proving that the sample has good immunity to interference. Similar phenomena can also be observed in the cases of Fe-PFM-30 and Ni-PFM-30, as the current responses produce by those common interferents are very little (Figs. S19b and S20b), demonstrating that both Fe-PFM-30 and Ni-PFM-30 have good anti-interference ability. In addition, the sensing performances of the Co-PFM-30 sensor under deformations (i.e., bending, recovery, and re-bending) towards 1 mM H_2O_2 are shown in Fig. S21. The change of response currents under different deformations is less than 5% with respect to that of the original status, indicating that the Co-PFM-30 sensor with good flexibility has stable performance and good strain resistance. The electrochemical stability of Co-PFM-30 is further measured in 0.1 M PBS containing 1 mM H_2O_2. As shown in Fig. 3f, the device exhibits a stable current response within 24 h. After that, Co-PFM-30 still shows a significant current response with the addition of 1 mM H_2O_2. In addition, the response currents at 0.6 V to H_2O_2 with concentrations of 0.2, 0.5, and 1 mM are recorded every 2 days (inset of Fig. 3f), and variations of the currents within 12 days is less than 5%, indicating that Co-PFM-30 electrode has good stability in the case of electrochemical sensing. Moreover, the reproducibility of Co-PFM-30 is firstly evaluated by repeatedly measuring 1 mM H_2O_2 for six times by using the same electrode. As shown in Fig. S22a, the overlap of the i-t curves indicates the identical current responses with a relative standard deviation (RSD) of 1.05% (inset of Fig. S22a). The XPS results in Fig. S23 further confirm that the structure and composition of Co-PFM-30 remain unchanged after six repeated H_2O_2 detections. The reproducibility of Co-PFM-30 is further assessed, and the response currents towards 1 mM H_2O_2 are measured by using six different electrodes (3 times for each electrode). The slight deviation in the response currents corresponds to a RSD of 2.27% (Fig. S22b). These results indicate good reproducibility and repeatability of Co-PFM-30 electrode. Moreover, the pH of wound exudates is different at different healing stages (Cui et al., 2022), and therefore, the sensing performance should be evaluated in environments with different pH. Fig. S24 shows the sensing performance of Co-PFM-30 for 1 mM H_2O_2 in PBS solutions with pH values of 7, 8, and 9. The overlap of the responses indicates that the change of pH of the wound exudates has neglectable influence on the sensing performance.

To further investigate the biocompatibility of the sensing platform, L929 cells are cultured with Co-PFM-30 extract for two days. The live/dead staining results indicate that the cells cultured with Co-PFM-30 show good status, regular morphology, and uniform size, and no significant cell apoptosis or necrosis is observed (Fig. S25a). In addition, the cell counting experiment also confirms the good biocompatibility of Co-PFM-30 (Fig. S25b). Moreover, we create a wound model on the

posterior back of experimental mouse for practical wound H_2O_2 concentration detection (Fig. S26a). The H_2O_2 concentration sensor is attached to the mouse skin injury at 0 and 2 h of the injury (Fig. S26b). The results show a significant change in the current after Co-PFM-30 is exposed to the mouse wound model, while there is no significant current change in the control group without wound model. The response current gradually diminished with increasing time (Fig. S26b), which might due to the self-healing of mouse wound, resulting in decreased H_2O_2 concentration. The current experiment demonstrates that the Co-PFM H_2O_2 sensor can be used for real-time monitoring of wound in practical circumstance, which has a positive effect for daily real-time monitoring and care treatment of chronic non-healing wounds.

To go deeper into the sensing mechanism, theoretical simulation was carried out to analyze the catalytic effect produced by Co ions anchored to ZIF-4 crystals. According to the XANES spectra of Co-PFM, Co ions are anchored to the ZIF-4 network structure mainly through Co–N and Co–Zn bonds. Since the Co–N unsaturated coordination bond is favorable for catalytic H_2O_2, Co ion attached to N atom was considered in the model to simplify the calculation (Du et al., 2023). Fig. 4a and b show the reaction paths of H_2O_2 on the surfaces of ZIF-4 and Co-PFM during the sensing process. For ZIF-4, H_2O_2 molecule first adsorbs on the Zn active sites, and then dissociates into hydroxyl groups, which also adsorbs on the active sites. Then, one of the hydroxyl groups desorbed from the Zn adsorption site, and the adsorbed hydroxyl group reacts with the

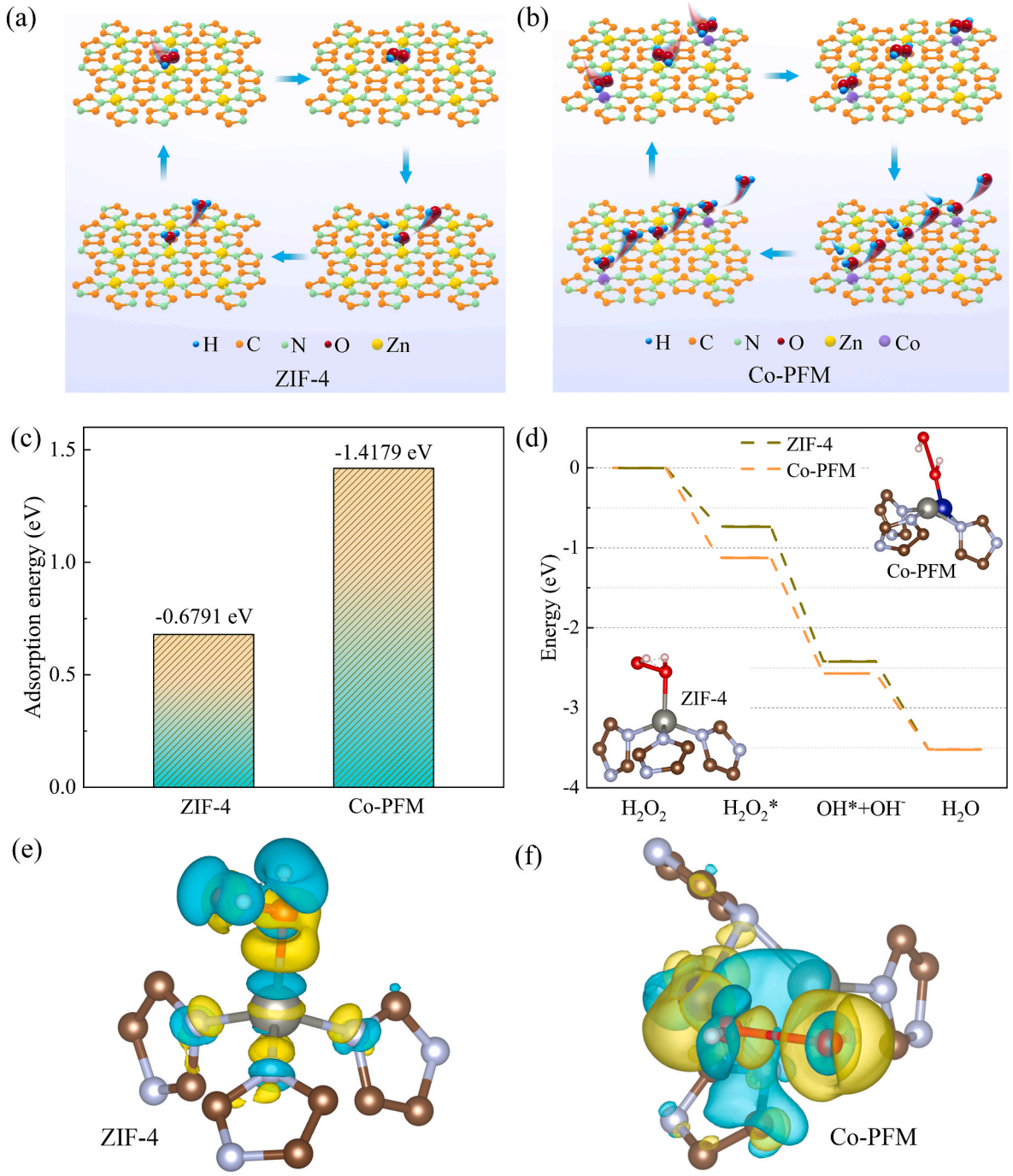

Fig. 4. Sensing mechanism of ion-implanted porous flexible films. Reaction paths of H_2O_2 on the surface of (a) ZIF-4 and (b) Co-PFM during the sensing process. (c) Corresponding adsorption energy of H_2O_2 on ZIF-4 and Co-PFM. (d) Free energy diagrams of the proposed reaction processes. The insets show the corresponding DFT calculation models. Differential charge density of H_2O_2 adsorbed on (e) ZIF-4 and (f) Co-PFM.

protonated hydrogen atom to produce an H_2O molecule adsorbed on the active sites. When the H_2O molecule desorbed, the catalyst substrate returns to its initial state (Chen et al., 2021). Co-PFM films have added new Co active site in addition to Zn active site, and the overall reaction path is the same. Thus, both Zn and Co are the active sites, and the number of active sites directly affects the sensing performance. However, the difference in the ability of the two active sites to decompose H_2O_2 needs to be further investigated. For this purpose, we perform DFT calculations to simulate the sensing mechanism (the optimized DFT calculation model is shown in Fig. S27). Adsorption and activation of H_2O_2 molecules on the active site is the first step of the sensing process which plays an important role in the subsequent reaction path. The adsorption energies of H_2O_2 molecules on ZIF-4 and Co-PFM are calculated, and the results in Fig. 4c show that the adsorption energies of the ZIF-4 and Co-PFM are −0.68 and −1.42 eV, respectively. The ability of the Co active sites to trap H_2O_2 molecules is demonstrated to be much higher than that of the Zn active sites. Fig. 4d shows the free energy diagrams of ZIF-4 and Co-PFM. One can see that the energy barrier of activating H_2O_2 for ZIF-4 is 0.44 eV, while the energy barrier decreases to 0.05 eV after Co implantation. It indicates that the presence of Co ions facilitates the decrease of the energy barrier of activating H_2O_2 and makes the reaction more likely to occur. For the reaction that catalyzes the production of reactive hydroxyl radicals from H_2O_2: $H_2O_2 \rightarrow H_2O_2^* \rightarrow OH^* + OH^-$, ZIF-4 releases 2.42 eV externally, while Co-PFM releases 2.57 eV externally. It elucidates that the ability of Co-PFM to catalyze the reaction is much higher than that of ZIF-4. Fig. 4e and f shows the differential charge density of H_2O_2-adsorbed ZIF-4 and Co-PFM respectively. The differential charge density charts show electrons loss in blue and gain in yellow, with the size of the electron cloud representing the range and intensity of charge transfer. Comparison of the electron cloud diagrams demonstrates that the charge transfer between H_2O_2 and Co active sites are stronger, further proving the stronger adsorption of H_2O_2 on Co active sites. Additionally, the O–O bond of H_2O_2 shows a significant charge interruption distribution at the Co active site, which makes H_2O_2 easily decompose to hydroxyl groups (Li et al., 2021b). Above all, the simulation shows that the introduction of Co ions not only leads to the strong adsorption of H_2O_2 molecules but also lowers the energy barrier of H_2O_2 activation. Therefore, intended ion design can greatly enhance the sensing performance.

4. Conclusion

In summary, the regulation of the biosensing properties of MOF film synthesized by gas-phase method is achieved by ion design via an implantation approach. The specific sensing of H_2O_2, DA, and glucose were realized by respectively anchoring Co, Fe, and Ni ions on porous network structure of ZIF-4 films. Specifically, Co-PFM enables high performance biosensing with a sensitivity of up to 2111 $\mu A\ mM^{-1}\ cm^{-2}$ and a linear range of 1–100 μM. The produced flexible biosensing device is capable of real-time monitoring H_2O_2 concentration at mouse wound. On the other hand, the sensitivity of the Fe-PFM and Ni-PFM are 2475 and 1669 $\mu A\ mM^{-1}\ cm^{-2}$ towards DA and glucose, respectively. Microstructural characterizations verify the chemical status of the ions in the MOF film and the simulation demonstrate that the ion design lead to enhanced electrochemical sensing performance. This study provides a new strategy for the properties regulation of MOF films by implanting desired metal ions, fueling them into multi-functional on-chip devices.

CRediT authorship contribution statement

Jinlong Wang: Writing – original draft, Visualization, Validation, Project administration, Methodology, Investigation, Data curation, Conceptualization. **Ji Tan:** Supervision, Resources, Project administration, Methodology, Data curation. **Zhe Zhao:** Software, Resources, Methodology, Conceptualization. **Jiayuan Huang:** Visualization, Validation, Software. **Junjie Zhou:** Validation, Methodology, Formal analysis. **Xinyi Ke:** Validation, Software, Project administration. **Zihan Lu:** Visualization, Investigation, Data curation. **Gaoshan Huang:** Writing – review & editing, Resources, Formal analysis, Conceptualization. **Hongqing Zhu:** Validation, Methodology, Formal analysis. **Xuanyong Liu:** Writing – review & editing, Software, Resources, Funding acquisition, Conceptualization. **Yongfeng Mei:** Writing – review & editing, Supervision, Software, Resources, Funding acquisition, Conceptualization.

Declaration of competing interest

The authors declare that they have no known competing financial interests or personal relationships that could have appeared to influence the work reported in this paper.

Data availability

Data will be made available on request.

Acknowledgements

This work is supported by the National Key Technologies R&D Program of China (2021YFA0715302 and 2021YFE0191800), the National Natural Science Foundation of China (52203328), the Science and Technology Commission of Shanghai Municipality (22ZR1405000).

Appendix A. Supplementary data

Supplementary data to this article can be found online at https://doi.org/10.1016/j.bios.2024.116433.

References

Ahmad, M., Nisar, A., Sun, H.Y., 2022. Biosensors 12 (11), 955.
Albetran, H.M., 2023. Materials 16 (4), 1749.
Biswas, S., Chen, Y.L., Xie, Y., Sun, X., Wang, Y., 2020. Anal. Chem. 92 (6), 4566–4572.
Calzaferri, G., Gallagher, S.H., Brühwiler, D., 2022. Microporous Mesoporous Mater. 330, 111563.
Charkhabi, S., Jackson, K.J., Beierle, A.M., Carr, A.R., Zellner, E.M., Reuel, N.F., 2021. ACS Sens. 6 (1), 111–122.
Chen, J., Li, G., Lu, N., Lin, H., Zhou, S., Liu, F., 2022a. Mater. Today Chem. 24, 100832.
Chen, K.F., Wang, X.L., Hu, W.H., Kong, Q.Q., Pang, H., Xu, Q., 2022b. Small Struct. 3, 2100200.
Chen, X., Dong, J.J., Chi, K., Wang, L.J., Xiao, F., Wang, S., Zhao, Y., Liu, Y.Q., 2021. Adv. Funct. Mater. 31, 2102855.
Chen, Y.N., Yang, Z.Q., Hu, H.L., Zhou, X.C., You, F., Yao, C., Liu, F.J., Yu, P., Wu, D., Yao, J.L., Hu, R.F., Jiang, X.L., Yang, H., 2022c. Front. Chem. 10, 881172.
Cui, H.Y., Liu, M.S., Yu, W.W., Cao, Y.F., Zhou, H.C., Yin, J.J., Liu, H.B., Que, S., Wang, J. J., Huang, C.S., Gong, C.L., Zhao, G.H., 2021. ACS Appl. Mater. Interfaces 13 (23), 26800–26807.
Cui, T.T., Yu, J.F., Wang, C.F., Chen, S., Li, Q., Guo, K., Qing, R.K., Wang, G.F., Ren, J.A., 2022. Adv. Sci. 9, 2201254.
Du, Y.X., Yang, Q., Lu, W.T., Guan, Q.Y., Cao, F.F., Zhang, G., 2023. Adv. Funct. Mater. 33, 2300895.
Elanjeitsenni, V.P., Vadivu, K.S., Prasanth, B.M., 2022. Mater. Res. Express 9, 022001.
Fu, X.C., Ding, B.W., D'Alessandro, D., 2023. Coord. Chem. Rev. 475, 214814.
Geng, D., Huang, Y.C., Yuan, S.F., Jiang, Y.Y., Ren, H., Zhang, S., Liu, Z., Feng, J., Wei, T., Fan, Z.J., 2023. Small 19, 2207227.
Ghafoor, M., Khan, Z.U., Nawaz, M.H., Akhtar, N., Rahim, A., Riaz, S., 2023. Environ. Monit. Assess. 195, 423.
Hao, J.X., Zhang, M.Q., Wu, C., Wu, K.B., 2021. Anal. Chim. Acta 1179, 338812.
Hao, J.X., Zhu, Z.Q., Hu, C.G., Liu, Z.H., 2022. Anal. Chem. 94 (10), 4547–4555.
Hu, J.S., Xu, Q.L., Wang, X.Y., Huang, X.H., Zhou, C.H., Ye, Y., Zhang, L., Pang, H., 2023. Carbon Energy 5, e315.
Hu, M.H., Korschelt, K., Daniel, P., Landfester, K., Tremel, W., Bannwarth, M.B., 2017. ACS Appl. Mater. Interfaces 9 (43), 38024–38031.
Jain, P., Kumari, G., Bhogra, M., Yanda, P., Joseph, B., Waghmare, U.V., Narayana, C., 2023. Inorg. Chem. 62 (20), 7703–7715.
Ji, L.D., Wang, J., Wu, K.B., Yang, N.J., 2018. Adv. Funct. Mater. 28, 1706961.
Jo, Y.M., Jo, Y.K., Lee, J.H., Jang, H.W., Hwang, I.S., Yoo, D., 2023. Adv. Mater. 35, 2206842.
Kekonen, A., Bergelin, M., Johansson, M., Joon, N.K., Bobacka, J., Viik, J., 2019. Sensors 19 (11), 2505.
Kim, S.J., Koh, H.J., Ren, C.E., Kwon, O., Maleski, K., Cho, S.Y., Anasori, B., Kim, C.K., Choi, Y.K., Kim, J., Gogotsi, Y., Jung, H.T., 2018. ACS Nano 12 (2), 986–993.
Li, C.F., Zhao, J.W., Xie, L.J., Wu, J.Q., Li, G.R., 2021a. Appl. Catal., B 282, 119463.

Li, H.L., Dong, F.Q., Bian, L., Huo, T.T., He, X.C., Zheng, F., Lv, Z.Z., Jiang, L.M., Li, B.W., 2021b. Colloids Surf., A 611, 125777.
Li, P.P., Bai, Y., Zhang, G.X., Guo, X.T., Meng, X.R., Pang, H., 2022. Inorg. Chem. Front. 9, 5853–5861.
Li, X., Wang, S.W., Chen, P., Xu, B.K., Zhang, X., Xu, Y.H., Zhou, R., Yu, Y., Zheng, H.L., Yu, P., Sun, Y.J., 2023a. Appl. Catal., B 325, 122401.
Li, Z.L., Deng, L.B., Kinloch, I.A., Young, R.J., 2023b. Prog. Mater. Sci. 135, 101089.
Lisse, T.S., Rieger, S., 2017. J. Cell Sci. 130, 975–988.
Liu, M., Hudson, Z.M., 2023. Adv. Funct. Mater. 33, 2214262.
Liu, X.Y., Zhang, Q., Li, M., Qin, S., Zhao, Z.Q., Lin, B., Ding, Y.M., Xiang, Y.T., Li, C.W., 2023. Environ. Res. 229, 115979.
Liu, Y., Yan, X.Y., Tang, Y.T., Lu, N.N., Zhang, T.T., Xu, Z.Q., Xing, Y., Zhao, P.Y., Liu, M. H., Zhu, Y.X., Zhang, Z.Q., Yang, M., 2022. J. Electroanal. Chem. 926, 116932.
Majhi, S.M., Ali, A., Rai, P., Greish, Y.E., Alzamly, A., Surya, S.G., Qamhieh, N., Mahmoud, S.T., 2022. Nanoscale Adv. 4, 697–732.
Nisar, A., Khan, M.A., Hussain, Z., 2022. J. Korean Ceram. Soc. 59, 359–369.
Raval, Y.S., Fleming, D., Mohamed, A., Karau, M.J., Mandrekar, J.N., Schuetz, A.N., Greenwood-Quaintance, K.E., Beyenal, H., Patel, R., 2023. Adv. Ther. 6, 2300059.
Rezki, M., Septiani, N.L.W., Iqbal, M., Adhika, D.R., Wenten, I.G., Yuliarto, B., 2022. J. Electrochem. Soc. 169, 017504.
Sarmah, N., Sharma, D., Mehta, B.K., Shrivastava, B.D., Das, B.K., Zimina, A., Gaur, A., 2022. J. Mol. Struct. 1263, 133125.
Schelch, S., Bolivar, J.M., Nidetzky, B., 2022. Biotechnol. Bioeng. 119, 2374–2387.
Shahsavari, M., Sheikhshoaie, I., Beitollahi, H., 2023. J. Food Meas. Char. 17, 1109–1118.
Shi, F., Xu, J.M., Hu, Z.F., Ren, C.L., Xue, Y.D., Zhang, Y.C., Li, J., Wang, C.Y., Yang, Z.J., 2021. Chin. Chem. Lett. 32, 3185–3188.
Shi, H., He, Y., Li, Y.B., Luo, P.Y., 2023a. J. Hazard Mater. 443, 130345.
Shi, Z.H., Weng, K.Y., Li, N., 2023b. Molecules 28 (1), 22.
Wang, J.M., Shao, D., Jiang, L.L., Li, H.X., Gao, Y.J., Rao, S.Q., Yang, Z.Q., 2022. J. Anal. Test. 6, 411–418.
Widmer, R.N., Lampronti, G.I., Chibani, S., Wilson, C.W., Anzellini, S., Farsang, S., Kleppe, A.K., Casati, N.P.M., MacLeod, S.G., Redfern, S.A.T., Coudert, F.X., Bennett, T.D., 2019. J. Am. Chem. Soc. 141 (23), 9330–9337.
Xia, Y.P., Shi, F., Liu, R.X., Zhu, H.B., Liu, K., Ren, C.L., Li, J., Yang, Z.J., 2024. Anal. Chem. 96 (3), 1345–1353.
Xie, J.Y., Zhang, X.Y., Yu, N., Luan, R.N., Zhang, D.Z., Zeng, J.B., Chai, Y.M., Dong, B., 2022. Mater. Today Phys. 27, 100778.
Yao, Y., Huang, W., Chen, J.H., Liu, X.X., Bai, L.B., Chen, W., Cheng, Y.H., Ping, J.F., Marks, T.J., Facchetti, A., 2023. Adv. Mater. 35, 2209906.
Yoo, S.K., Starnes, T.W., Deng, Q., Huttenlocher, A., 2011. Nature 480, 109–112.
Yuan, Y.A., Wang, L.L., Cui, X.J., Peng, F., 2023. Mod. Phys. Lett. B 37, 2250211.
Zhang, H.Y., Xu, G.Q., Chen, Y.M., Li, X., Wang, S.P., Jiang, F.H., Zhan, P.Y., Lu, C.F., Cao, X.D., Ye, Y.K., Tao, Y.L., 2023a. Sensors 23 (9), 4396.
Zhang, J.W., Li, C.L., Wang, H., Yang, Z., Hu, C.G., Wu, K.B., Hao, J.X., Liu, Z.H., 2023b. Anal. Chem. 95 (51), 18907–18916.
Zhang, S.P., Rana, S.S., Bhatta, T., Pradhan, G.B., Sharma, S., Song, H.Y.S., Jeong, S., Park, J.Y., 2023c. Nano Energy 106, 108110.
Zhao, R., Liang, Z.B., Zou, R.Q., Xu, Q., 2018. Joule 2, 2235–2259.
Zhao, W.S., Li, G.D., Tang, Z.Y., 2019. Nano Today 27, 178–197.
Zhao, Z., Kong, Y., Huang, G.S., Liu, C., You, C.Y., Xiao, Z.J., Zhu, H.Q., Tan, J., Xu, B.R., Cui, J.Z., Liu, X.Y., Mei, Y.F., 2022. Nano Today 42, 101347.
Zhao, Z., Kong, Y., Lin, X.Y., Liu, C., Liu, J.R., He, Y.Y., Yang, L.L., Huang, G.S., Mei, Y.F., 2020. J. Mater. Chem. A 8, 26119–26129.
Zhou, H.J., Zhu, G.Y., Dong, S.Y., Liu, P., Lu, Y.Y., Zhou, Z., Cao, S., Zhang, Y.Z., Pang, H., 2023. Adv. Mater. 35, 2211523.
Zuo, Q., Cui, R., Wang, L., Wang, Y.L., Yu, C.Y., Wu, L., Mai, Y.Y., Zhou, Y.F., 2023. Sci. China: Chem. 66, 570–577.